



**HAL**  
open science

## Impact of excavation damage on the thermo-hydro-mechanical properties of natural Boom Clay

Linh-Quyen Dao, Yu-Jun Cui, Anh Minh A.M. Tang, Jean-Michel Pereira,  
Xiang-Ling Li, Xavier Sillen

► **To cite this version:**

Linh-Quyen Dao, Yu-Jun Cui, Anh Minh A.M. Tang, Jean-Michel Pereira, Xiang-Ling Li, et al..  
Impact of excavation damage on the thermo-hydro-mechanical properties of natural Boom Clay. En-  
gineering Geology, 2015, 195, pp.196-205. 10.1016/j.enggeo.2015.06.011 . hal-01271302

**HAL Id: hal-01271302**

**<https://enpc.hal.science/hal-01271302v1>**

Submitted on 25 Apr 2018

**HAL** is a multi-disciplinary open access archive for the deposit and dissemination of scientific research documents, whether they are published or not. The documents may come from teaching and research institutions in France or abroad, or from public or private research centers.

L'archive ouverte pluridisciplinaire **HAL**, est destinée au dépôt et à la diffusion de documents scientifiques de niveau recherche, publiés ou non, émanant des établissements d'enseignement et de recherche français ou étrangers, des laboratoires publics ou privés.

1 **Impact of excavation damage on the thermo-hydro-mechanical**  
2 **properties of natural Boom Clay**

3 Linh-Quyen DAO <sup>1</sup>, Yu-Jun CUI <sup>1</sup>, Anh-Minh TANG <sup>1</sup>, Jean-Michel PEREIRA <sup>1</sup>, Xiang-Ling LI <sup>2</sup>, Xavier  
4 SILLEN <sup>3</sup>

5 <sup>1</sup> Ecole des Ponts ParisTech, Navier/CERMES, Marne la Vallée, France

6 <sup>2</sup> European Underground Research Infrastructure for Disposal of nuclear waste In Clay Environment, ESV EURIDICE GIE, Mol,  
7 Belgium

8 <sup>3</sup> Belgian Agency for Radioactive Waste and Enriched Fissile Materials (ONDRAF/NIRAS), Brussels, Belgium

9

10

11

12

13

14

15

16

17

18

19 **Corresponding author:**

20 Prof. Yu-Jun CUI

21 Ecole des Ponts ParisTech

22 6-8 av. Blaise Pascal, Cité Descartes, Champs-sur-Marne

23 77455 Marne-la-Vallée cedex 2

24 France

25

26 Email: yujun.cui@enpc.fr

27 Phone: +33 1 64 15 35 50

28 Fax: +33 1 64 15 35 62

29

30 **Abstract**

31 Boom Clay has been considered as a potential host-rock for the geological radioactive waste disposal in  
32 Belgium. In this context, it is important to well understand its thermo-hydro-mechanical behaviour around  
33 the disposal galleries. In this study, the effect of excavation damage on the thermo-hydro-mechanical  
34 properties of natural Boom Clay around the Connecting gallery (excavated in 2002) in the Mol  
35 underground Research Laboratory HADES (High-Activity Disposal Experimental Site) was investigated.  
36 Several samples taken from a horizontal borehole drilled in July 2012 were tested. The thermal  
37 conductivity in three different orientations (perpendicular, parallel, and 45° to the bedding plane) were  
38 measured using the needle probe method. The results show a cross-anisotropy of natural Boom Clay and  
39 an impact of the excavation damage on the thermal property of samples near the gallery. To further  
40 investigate the anisotropy behaviour, bender element tests were carried out under unconfined conditions  
41 to determine the small-strain shear modulus also in three different orientations. The obtained results  
42 confirm the anisotropic behaviour of Boom Clay. Moreover, the evolution of small-strain modulus with the  
43 distance from the gallery axis ( $r$ ) was found to be similar to that of thermal conductivity: the values in the  
44 zone near the gallery are lower than those in the far field. From these experimental data, an extent of the  
45 excavation damaged zone (EDZ) of 4 m from the connecting gallery axis was determined. Further  
46 investigations on the microstructure of several samples taken at different distances  $r$  by mercury intrusion  
47 porosimetry (MIP) and scanning electron microscope (SEM) methods were carried out. Macro-pores of  
48 diameter  $\geq 5 \mu\text{m}$  were identified in the samples near the gallery. The identified macro-pores were related  
49 to the effect of excavation damage, and a damage variable was thus defined, allowing a damage model to  
50 be developed. The values of the two model parameters have been determined from the observed  
51 relationship between macro-porosity and thermal conductivity. Comparisons between predicted and  
52 experimental results in terms of small strain shear modulus and hydraulic conductivity have shown  
53 reasonable agreement.

54 Keywords: Boom Clay; excavation damage; thermal conductivity, shear modulus, microstructure;  
55 anisotropy

56

57

58

59

60

61

62

63

## 65 1. Introduction

66 Geological formation of stiff clays or Claystone is often considered as potential host formation for the  
67 radioactive waste disposal at great depth. In Europe, several Underground Research Laboratories (URLs)  
68 have been constructed in stiff clay/Claystone formations such as the HADES URL (Belgium) in Boom  
69 Clay, Mont Terri URL (Switzerland) in Opalinus Clay, Bure URL (France) in Callovo-Oxfordian Claystone,  
70 etc. In this context, the damaged or disturbed zone around the gallery due to excavation is one of the most  
71 important research issues. This zone has several names and definitions depending on the research  
72 programs (Lanyon, 2011). According to Tsang and Bernier (2004), Tsang et al. (2005), Bastiaens et al.  
73 (2007), and Lanyon (2011), this zone is defined as the excavation damaged zone (EDZ) where the hydro-  
74 mechanical and geochemical modifications induced by the excavation lead to significant changes in flow  
75 and transport properties. For instance, these changes can be characterised by an increase of several  
76 magnitudes in hydraulic conductivity.

77 The characterisation of EDZ was investigated experimentally for several host formations such as Boom  
78 Clay (Mertens et al., 2004), Callovo-Oxfordian Claystone (Armand et al., 2007), Opalinus Clay (Popp et  
79 al., 2008). Depending on the host formation properties, time and budget, the characterisation method can  
80 be different (Lanyon, 2011). In order to investigate the fractures/damage induced by excavation and the  
81 lithology changes, borehole core drilling and logging are often used. The extent of EDZ can be identified  
82 by the changes in matrix geophysical and hydromechanical properties that are determined by the tests on  
83 the borehole cores. For instance, Matray et al. (2007) determined the EDZ extent in Tournemire's argillite  
84 (France) through changes in degree of saturation; Autio et al. (1998) did that in Äspö Hard Rock (Sweden)  
85 through changes in porosity.

86 During the excavation of Connecting Gallery (diameter 4.8 m) in HADES URL, fractures were intensively  
87 investigated. (Bastiaens et al., 2003; Mertens et al., 2004). The fracture pattern consists of two conjugated  
88 curved planes and the extent of the fractured zone in the horizontal direction is larger than that in the  
89 vertical one. Two cored borings, one horizontal and one vertical, were performed shortly after the  
90 construction of the Connecting gallery to assess the radial extent of the fractures. Fractures presumably  
91 related to the excavation were found up to about 1 metre in the horizontal core and up to about 0.6 m in the  
92 vertical core (Bernier et al., 2006). Charlier et al. (2010) analysed the extent of plastic zone developed  
93 around the gallery of PRACLAY (diameter 2.5m) at the end of excavation through numerical simulations in  
94 2D, axisymmetric and 3D conditions, and the obtained results are in good agreement with the field  
95 observation: depending on the values adopted for the parameters of the constitutive model, the calculated  
96 plastic zone can extend up to about 3 m in the vertical direction and about 10 m in the horizontal direction  
97 when considering material anisotropy.

98 Mertens et al. (2004) reported a seismic campaign performed in two parallel horizontal boreholes 2000–4  
99 and 2000–5 in the Mounting Chamber from the Connecting gallery of the HADES URL in order to identify

100 the extent of EDZ. These two boreholes have a distance of 3.6 m from each other. The velocity of  
101 compression wave  $V_p$  was measured using a mini-sonic probe. Significant data scatter was observed in  
102 the zone up to about 2 m from the gallery extrados, i.e. the outer surface of the gallery's wall (2.8 m in  
103 2000–4 and 1 m in 2000–5), suggesting significant damage of this zone.

104 Another in-situ measure allowing the characterisation of the EDZ around the Connecting gallery is the  
105 hydraulic conductivity ( $k$ ). Yu et al. (2011a) reported a large investigation over 30 years on the hydraulic  
106 conductivity of Boom Clay. Some data involve the evolution of hydraulic conductivity with the distance  
107 from the gallery extrados. For instance, two piezometers equipped with pressure controller and high-  
108 definition balance were installed: R55D (vertical) and R55E (horizontal). The measurement obtained from  
109 the vertical piezometer is mainly the contribution of  $k_h$  or  $k_{//}$  (hydraulic conductivity parallel to the bedding  
110 plane), while the measurement obtained from the horizontal piezometer ( $k_g$ ) is the combined contribution  
111 of  $k_{\perp}$  (hydraulic conductivity perpendicular to the bedding plane) and  $k_{//}$  (Yu et al., 2013a). The relation  
112 between  $k_g$ ,  $k_{\perp}$  and  $k_{//}$  after Roy (1991) is:

$$k_g = \sqrt{k_{\perp} \cdot k_{//}} \quad (1)$$

113 Using Eq. (1), the vertical hydraulic conductivity can be deduced using the measurements from the vertical  
114 and horizontal piezometers. The obtained results show that the hydraulic conductivity is strongly disturbed  
115 in the zone of 6 m from the gallery's wall. This extent is larger than that deduced from  $V_p$  measurements  
116 (2 m from the gallery's wall).

117 Several studies showed that the EDZ in Boom Clay can be sealed after a certain time, with a hydraulic  
118 behaviour that becomes close to that of intact Boom Clay (Bastiaens et al., 2007; Mertens et al., 2002).  
119 On the other hand, healing, i.e. restoration of original mechanical properties, has not been demonstrated.  
120 This aspect was investigated in this study by testing Boom Clay cores taken 10 years after the gallery  
121 excavation (2002). The EDZ extent was appreciated based on changes in small-strain shear modulus ( $G_0$ )  
122 and thermal conductivity ( $\lambda$ ). Different directions with respect to the bedding plane were considered,  
123 allowing the anisotropic behaviour to be studied. Furthermore, microstructure changes were also  
124 analysed, allowing identification of the creation of a population of macro-pores that was due to the  
125 excavation damage. A parameter related to these macro-pores was then defined, allowing description of  
126 the effect of excavation damage on the thermo-hydro-mechanical properties (i.e. thermal conductivity -  $\lambda$ ,  
127 small-strain shear modulus -  $G_0$  and hydraulic conductivity -  $k$ ) of Boom Clay.

128

## 129 **2. Materials and methods**

### 130 **2.1. Materials**

131 Boom Clay is located in the North of Belgium at depth between 185 m and 287 m at Mol (Mertens et al.,  
132 2004). Its bedding plane is considered to be almost horizontal; its layer is gently dipping ( $\pm 1^\circ$ ) toward the  
133 North-North-East (Mertens et al. 2003). This material mainly consists of clay minerals dominated by

134 kaolinite and illite (Lima, 2011, Dehandschutter et al., 2005). In this study, several samples were taken  
 135 from a horizontal borehole (R66-67) of 100 mm diameter (the axis is parallel to the bedding plane). This  
 136 borehole was drilled in July 2012 from the connecting gallery which was excavated in 2002 with 4.0 m  
 137 diameter and 0.4 m thick liner. The full code of the borehole or cores is: Boom Clay / Mol Site / HADES  
 138 borehole 2012-2 / Connecting gallery / Ring 66-67W / 0.40 m to 20.3 m from the intrados of the lining.  
 139 After being extracted, each core sample was vacuum-packaged in aluminium foil to minimise water loss  
 140 by evaporation.

141 The initial suction of Boom Clay after opening these aluminium foils was measured using a dew-point  
 142 hygrometer and a value of about 3 MPa was obtained which is close to that estimated by Delage et al.  
 143 (2007). Other parameters such as water content ( $w$ ), degree of saturation ( $S_r$ ) were also measured.  
 144 Further examination shows that the relationship between suction and water content was in good  
 145 agreement with the retention curve reported by Delage et al. (2007).

146

## 147 2.2. Thermal conductivity measurement

148 After trimming from core, the samples (100 mm in diameter and 60 mm - 90 mm in height) were then  
 149 slightly confined by means of an adhesive tape so as to avoid further crack propagation and any  
 150 perturbation. The thermal conductivities of natural Boom Clay in three orientations (parallel, perpendicular  
 151 and 45° to the bedding plane) were measured using a thermal needle probe - KD2 Pro. A single needle  
 152 (60 mm in length, 1.3 mm in diameter) was inserted into the soil specimen (Figure 1). In this needle probe  
 153 method (or line source method), the theory of axisymmetric heat diffusion from an infinite line source  
 154 within an infinite surrounding medium was used. Hence, a radial heat flow is produced within the  
 155 specimen while measuring temperature changes over time. More details can be seen in Tang et al.  
 156 (2008). In order to measure the thermal conductivity in three orientations, three holes were drilled in each  
 157 sample in order to vary the angle  $\theta$  between the axis of needle probe and the bedding plane ( $\theta = 0^\circ, 45^\circ,$   
 158  $90^\circ$ ) (see Figure 1). Note that in the case of  $\theta = 90^\circ$ , the measured thermal conductivity  $\lambda_{90}$  is not the value  
 159 in the direction perpendicular to the bedding plane ( $\lambda_{\perp}$ ). The true value of  $\lambda_{\perp}$  is back-calculated from  $\lambda_{//}$  (or  
 160  $\lambda_0$ ) and the apparent thermal conductivity  $\lambda_{90}$  using Eq. (2) (Penner, 1963):

$$\lambda_{\perp} = \frac{(\lambda_{90})^2}{\lambda_0} \quad (2)$$

161 As the samples used were at unsaturated state, Johansen's method (Farouki, 1986) for fine unfrozen soils  
 162 was used to calculate the thermal conductivity at saturated state ( $\lambda_{sat}$ ) from the thermal conductivity at  
 163 unsaturated state ( $\lambda$ ) and dry state ( $\lambda_{dry}$ ) (Eq. (3)):

$$\lambda_{sat} = \frac{(\lambda - \lambda_{dry})}{K_e} + \lambda_{dry} \quad (3)$$

164 where

$$K_e \cong \log S_r + 1.0 \quad (4)$$

$$\lambda_{dry} = \frac{0.135\gamma_d + 64.7}{2700 - 0.947\gamma_d} \pm 20\% \text{ (W / mK)} \quad (5)$$

165 where  $\gamma_d$  is the dry density expressed in  $\text{kg/m}^3$ .

166

### 167 **2.3. Shear modulus measurement**

168 The small-strain shear modulus ( $G_0$ ) in different orientations of natural Boom Clay was determined by  
 169 performing bender elements tests under unconfined conditions. In a bender element test, the velocity of  
 170 shear wave ( $V_s$ ) is determined allowing calculation of the small-strain shear modulus ( $G_0$ ). The  
 171 experimental set-up used is depicted in Figure 2 (only soil sample and the transmitter are presented). The  
 172 receiver placed under the soil sample is not sketched in this figure.

173 For each sample (100 mm in diameter and 55 mm - 80 mm in height), the shear wave in three different  
 174 orientations ( $V_{hv}$ ,  $V_{hh}$ ,  $V_{h45}$ ) were generated by letting vibrate the transmitter element in the direction  
 175 perpendicular, parallel and at  $45^\circ$  with respect to the bedding plane. Note also that the direction of wave  
 176 propagation is always parallel to the bedding (see Figure 2). The travel times ( $\Delta t$ ) of shear wave was  
 177 determined. Then three small-strain shear modulus  $G_{hv}$ ,  $G_{hh}$ ,  $G_{h45}$  were calculated using Eq. (6) (Zeng and  
 178 Ni, 1999):

$$G_{0(ij)} = \rho V_{s(ij)}^2 \quad (6)$$

179 where  $i$  and  $j$  are the directions of shear wave propagation and particle vibration in the  $\sigma_i - \sigma_j$  plane,  
 180 respectively;  $\rho$  is the total density of soil ( $\text{Mg/m}^3$ );  $G_0$  is small-strain shear modulus (kPa),  $V_s$  is shear wave  
 181 velocity (m/s) determined by Eq. (7):

$$V_s = \frac{l}{\Delta t} \quad (7)$$

182 where  $l$  is the travel length of shear wave.

183 Note that the samples used for the bender element tests were the same as those used in the thermal  
 184 conductivity tests. Note also that the water content in these cores slightly decreased during the  
 185 conservation in the laboratory, resulting in an increase in suction. The values range from 3 MPa (suction  
 186 measured during thermal conductivity tests) to 5 MPa (suction measured during the bender element  
 187 tests).

188

### 189 **2.4. Microstructural investigations**

190 Two microstructural observation methods were used: scanning Electron Microscopy (SEM) and Mercury  
191 Intrusion Porosimetry (MIP). Note that the samples were freeze-dried prior to observations to minimise the  
192 modification of soil microstructure (Delage and Pellerin, 1984). The MIP tests were performed on an  
193 “AutoPore IV 9500 – Micromeritics Instrument Corp”. This equipment has two stages of pressure  
194 application. In the first stage, the equipment performs mercury intrusion at low pressures in the range  
195 between 0.0035 and 0.2 MPa, and measuring apparent pore diameters between 400  $\mu\text{m}$  and 3  $\mu\text{m}$ . In the  
196 second stage, the high-pressure is applied between 0.2 and 227.5 MPa, measuring pores diameters  
197 ranging from 3  $\mu\text{m}$  to 0.005  $\mu\text{m}$ .

198

### 199 3. Experimental results

#### 200 3.1. Shear stiffness and thermal conductivity

201 The variations of  $G_{\text{hv}}$ ,  $G_{\text{h45}}$ ,  $G_{\text{hh}}$  with the distance  $r$  from the axis of gallery for each sample are presented  
202 in Figure 3. It appears that  $G_{\text{hh}}$  displays a clear trend with distance  $r$ : It stabilises at 1450 MPa in the zone  
203 far from the gallery, decreases to 1200 MPa at  $r = 4$  m and then drops to 800 MPa at  $r = 2.5$  m. For  $G_{\text{hv}}$ ,  
204 except two values (638 MPa at  $r = 2.7$  m and 1403 MPa at  $r = 3.8$  m), a significant decrease is identified  
205 from the far field (1200 MPa at  $r = 9.2$  m) to the near field (808 MPa at  $r = 2.5$  m). The value of  $G_{\text{hv}}$  at  $r =$   
206 16 m is equal to the value of  $G_{\text{hh}}$ . This is quite surprising because  $G_{\text{hv}}$  is expected to be lower than  $G_{\text{hh}}$  due  
207 to the cross-anisotropy of Boom Clay formation. For  $G_{\text{h45}}$ , except two values at  $r = 4$  m (1098 MPa) and  $r =$   
208 16 m (1009 MPa), it seems to stabilise around 1300 MPa at the distance  $r$  from 3.8 m to 9.2 m, then  
209 decreases to 1066 MPa at  $r = 2.5$  m. In spite of the irregular evolutions of  $G_{\text{hv}}$  and  $G_{\text{h45}}$ , it appears clearly  
210 that the shear stiffness of the zone near the gallery  $r < 4$  m (about 1.6 m from the gallery extrados) is  
211 lower than that in the far field. It is also found that the obtained values of  $G_{\text{hv}}$  and  $G_{\text{hh}}$  in the far field are in  
212 good agreement with those obtained by Lima (2011) under unconfined condition ( $G_{\text{hh}} = 1483$  MPa and  $G_{\text{vh}}$   
213 = 1135 MPa). Areias et al. (2012) also measured the shear wave velocity in the field and obtained a value  
214 of  $V_s$  around 800 m/s that corresponds to a value of  $G_0$  of 1280 MPa. This is in agreement with the value  
215 obtained in this study.

216 The results of thermal conductivity at saturated state in the directions parallel ( $\lambda_{//}$  measured),  
217 perpendicular ( $\lambda_{\perp}$  calculated) and  $45^\circ$  ( $\lambda_{45}$  measured) to the bedding plane are shown in Figure 4 versus  
218 the distance  $r$  from the axis of gallery. For the  $\lambda_{//}$  measured, the value stabilises at 1.6 W/(m.K) in the zone  
219 far from the gallery then drops to 1.46 W/(m.K) at  $r = 3.4$  m and afterwards quickly decreases to 1.3  
220 W/(m.K) at  $r = 2.5$  m. The value of  $\lambda_{//}$  in the far field ( $r > 4$  m) is close to that found by Chen et al. (2011)  
221 by back analysis of a metre-scale in situ heater test (1.65 W/(m.K)). The variation trend of  $\lambda_{45}$  is similar to  
222 that of  $\lambda_{//}$ : the value stabilises at 1.5 W/(m.K) then quickly decreases to 1.2 W/(m.K) at  $r = 2.5$  m. For  $\lambda_{\perp}$   
223 calculated, the variation is not as regular as for  $\lambda_{//}$  and  $\lambda_{45}$ : the value in the far field varies slightly between  
224 0.95 and 1.05 W/(m.K), drops down to 0.8 W/(m.K) at  $r = 2.7$  m then increases to 0.9 W/(m.K) at  $r = 2.5$  m.  
225 From the measurements of thermal conductivity and small-strain shear modulus, the lasting influence of



226 excavation damage is confirmed, even more than 10 years after the excavation, at least on thermal-  
227 mechanical properties of unconfined samples.

228

### 229 **3.2. Microstructural investigation**

230 Mercury Intrusion Porosity (MIP) and Scanning Electron Microscopy (SEM) tests were carried out on  
231 several Boom Clay samples located at three distances  $r$  (2.5 m, 2.7 m and 9.2 m) to the gallery axis. The  
232 microstructural investigations were performed after measuring the thermal conductivity and the shear  
233 modulus. The bedding plane of Boom Clay can be detected at macroscopic scale as shown in Figure 5.  
234 The physical properties of Boom Clay samples used for MIP and SEM tests can be found in Table 1.  
235 Figure 6 shows the pore size distribution curves for the three samples. From pore size 5 nm to 5000 nm  
236 (i.e. 5  $\mu\text{m}$ ), the curves have a similar shape (Figure 6a) with a well-defined pore population at 80 nm. This  
237 observation is consistent with that by Lima (2011) and Nguyen (2013). The curves also revealed that  
238 these samples have almost no pores in the range from 1  $\mu\text{m}$  and 5  $\mu\text{m}$ . However, for the range beyond 5  
239  $\mu\text{m}$ , the two samples located near the gallery's wall ( $r = 2.5$  m and  $r = 2.7$  m respectively) show the  
240 presence of macro-pores, with the macro-pores being more pronounced for the sample which is closest to  
241 the gallery -  $r = 2.5$  m. These macro-pores could be related to the fissures created by the gallery  
242 excavation or to the excavation damage. It is also observed from Figure 6b that the final value of the  
243 intruded mercury void ratio (mercury intruded volume/volume of soil particles) for the three samples are  
244 always lower than their corresponding global soil void ratio  $e$  (see Table 1) due to non-intruded porosity  
245 (Lima, 2011).

246 To further evaluate the soil behaviour at microscopic level, the intruded mercury void ratio of macro-pore  
247  $e_M$  is used, which is the ratio of the mercury intruded volume of macro pore  $V_M$  to the volume of soil  
248 particles  $V_s$  (Eq. (8)):

$$e_M = \frac{V_M}{V_s} \quad (8)$$

249 The  $e_M$  of the Boom Clay samples is estimated by using the curves  $e_M - D$  (Figure 6b). For the three  
250 samples tested:  $e_M = 0.05$  ( $r = 2.5$  m);  $e_M = 0.02$  ( $r = 2.7$  m);  $e_M = 0.01$  ( $r = 9.2$  m). Figure 7 shows the  
251 evolution of  $e_M$  with distance  $r$ . It can be observed that the nearest sample to the gallery ( $r = 2.5$  m) has  
252 the maximum value of  $e_M$ , and the sample at  $r = 9.2$  m has the minimum.

253 The pore size distribution analysis was completed by the SEM observation. The views perpendicular and  
254 parallel to the bedding plane for the samples taken from three different distances,  $r = 2.5$  m, 2.7 m and 9.2  
255 m, are shown in Figure 8, Figure 9 and Figure 10, respectively. For the sample located at  $r = 2.5$  m, two  
256 photographs were taken at two dimensions: 1800 x 1400  $\mu\text{m}$  (Figure 8a), 1500 x 1100  $\mu\text{m}$  (Figure 8b). In  
257 Figure 8a, the beam of electron of microscope being parallel to the bedding plane, the bedding plane was  
258 clearly identified. In addition, a crack of about 50  $\mu\text{m}$  wide parallel to the bedding plane is detected. In  
259 Figure 8b, the beam of electron of microscope being perpendicular to the bedding plane, hence several

260 clay platelets parallel to each other are observed, without the presence of large cracks. From the pore size  
261 distribution curve at  $r = 2.5$  m (Figure 6a), macro-pores are observed in the range from  $10 \mu\text{m}$  to  $100 \mu\text{m}$ .  
262 The crack identified in Figure 8a corresponds to these identified macro-pores.

263 The SEM photographs of the second sample located at  $r = 2.7$  m are presented in Figure 9. When  
264 focusing the beam of electron parallel to the bedding plane (Figure 9a), the bedding plane is still well  
265 detected. Moreover, a crack as large as  $40 \mu\text{m}$  and parallel to the bedding plane is also observed. In  
266 Figure 9b, as the dimensions picture are smaller ( $850 \times 650 \mu\text{m}$ ) that that of Figure 8b, clay platelets are  
267 identified more clearly: they are superimposed upon each other. For this sample, the pore size distribution  
268 curve (Figure 6a) also shows some macro-pores of  $10 \mu\text{m}$  to  $100 \mu\text{m}$ . This is also in good agreement with  
269 the crack observed in Figure 9a.

270 For the sample located far from the gallery ( $r = 9.2$  m), two photographs at two scales were taken:  $2300 \times$   
271  $1800 \mu\text{m}$  (Figure 10a with the beam of electron parallel to the bedding plane) and  $640 \times 500 \mu\text{m}$  (Figure  
272 10b with the beam of electron perpendicular to the bedding plane). Although the dimensions of Figure 10a  
273 are close to those of Figure 6a and Figure 8a, only the bedding plane is detected and no crack is found.  
274 As the dimension of Figure 10b is slightly smaller than that of Figure 9b, several bedding planes are  
275 clearly observed.

276 Summarising, there is a good agreement between the MIP and SEM analyses, suggesting that the void  
277 ratio of macro-pore  $e_M$  (diameter  $\geq 5 \mu\text{m}$ ) is due to excavation damage. In other words, the excavation  
278 damage zone still exists even more than 10 years after the excavation. There are certainly some  
279 desiccation cracks after the sample has been taken out of the borehole. But the others results on Boom  
280 Clay samples at the “perfect” state (far field and undamaged condition) didn’t show the cracks with the  
281 same dimension and density.

282

## 283 **4. Prediction of thermo-hydro-mechanical properties**

### 284 **4.1. Damage variable**

285 Many theories of continuous damage mechanics were developed based on the concept of effective stress  
286 of Kachanov (1958) (see (Ambroziak, 2007; Gross and Seelig, 2011)). It is assumed that the relationship  
287 between the effective stress in the damaged material ( $\sigma_{ij}^*$ ) and that of the undamaged material ( $\sigma_{ij}$ ) is  
288 defined by a damage variable  $D$  (Eq. (9)):

$$\sigma_{ij}^* = \frac{\sigma_{ij}}{1-D} \quad (9)$$

289 For a linear elastic material, the amount of damage can be determined by Eq. (10):

$$D = 1 - \frac{E^*}{E} \quad (10)$$

290 where  $E$  is the Young's modulus of undamaged material,  $E^*$  is the Young modulus of damaged material.

291 In this study, as a decrease of thermal conductivity and small-strain shear modulus has been identified in  
 292 the location near the galley and this decrease is related to the excavation damage characterised by the  
 293 creation of macro-pores, a semi-empirical expression can be proposed to estimate the effect of excavation  
 294 damage on the properties of Boom Clay (see Eq. (11)). In this expression, parameter  $e_M$  defined by the  
 295 pores larger than 5  $\mu\text{m}$  is used as a measure of damage levels:

$$X = X_0 \left(1 - b \exp\left(-a \frac{e}{e_M}\right)\right) \quad (11)$$

296 where  $X_0$  is the property of Boom Clay in the far field (intact zone),  $X$  is the property of Boom Clay in the  
 297 near field (EDZ),  $e$  is the global void ratio (see Table 1). In this empirical equation, the damage variable  
 298 considered is the ratio between  $e$  and  $e_M$ .

299 In Eq. (11), there are two parameters to be determined:  $a > 0$  is a parameter depending on the material  
 300 and  $b$  is a parameter depending on the property considered ( $b > 0$  if the property of material decreases  
 301 with the increase of macro-pores;  $b < 0$  if the property of material increases with the increase of macro-  
 302 pores). Note that the derived fitting parameters  $a$  and  $b$  have no physical meaning. They just serve to get a  
 303 good agreement between the laboratory or field values and the modelled values. Thus, this modelling is  
 304 not based on hydraulic and/or mechanical processes.

#### 305 **4.2. Determination of parameters**

306 For Boom Clay, the results of thermal conductivity measurements are used to determine the two  
 307 parameters  $a$  and  $b$  by comparing the modelled and experimental results. For this purpose, the values of  
 308  $\lambda_{\perp}$ ,  $\lambda_{45}$ ,  $\lambda_{\parallel}$  in the far field (1.1 W/(m.K), 1.5 W/(m.K), 1.65 W/(m.K) respectively, see Table 2) are chosen to  
 309 compute the thermal conductivity at three distance  $r = 2.5$  m, 2.7 m and 9.2 m. With  $a = 0.05$  and  $b = 0.5$ ,  
 310 a good agreement is obtained between the model prediction and experimental results (Figure 4).

311 The same model is used to predict the small-strain shear modulus ( $G_{hv}$ ,  $G_{h45}$ ,  $G_{hh}$ ) located at three  
 312 different distances:  $r = 2.5$  m, 2.7 m and 9.2 m. As for the thermal conductivity, the values of  $G_{hv}$ ,  $G_{h45}$ ,  $G_{hh}$   
 313 in the intact zone and presented in Table 2 are used in the calculations. The predicted results with the  
 314 same parameters ( $a = 0.05$  and  $b = 0.5$ ) are compared to that measured in the laboratory in Figure 3. A  
 315 good agreement is also obtained. Note that the experimental values of thermal conductivity and small-  
 316 strain shear modulus at these three distances  $r$  are presented in Table 1.

317

#### 318 **4.3. Application of the damage model to the hydraulic property**

319 In order to verify this damage model for the hydraulic property of natural Boom Clay, the field hydraulic  
320 conductivity measurements in 2004 and 2005 (reported by Yu et al., 2011) and those obtained from the  
321 same piezometers R55D and R55E in 2012 (taken from the internal report of EURIDICE) are analysed.

322 The results of hydraulic conductivity  $k$  measurements in 2004, 2005 and 2012 are presented in Figure 11.  
323 Due to the excavation damage in the zone near the gallery, the hydraulic conductivity is quite high in this  
324 zone. The extent of EDZ, where the hydraulic conductivity is disturbed, reaches 6 m from the gallery  
325 extrados. Out of the EDZ, the values are about  $6.5 \cdot 10^{-12}$  m/s for  $k_{//}$  and at  $3.5 \cdot 10^{-12}$  m/s for  $k_{\perp}$  (computed  
326 from  $k_g$  and  $k_{//}$  using Eq. (1)). Comparison between the results of 2004, 2005 and 2012 shows that the  
327 influence of excavation on the hydraulic conductivity in the direction parallel to the bedding plane ( $k_{//}$ ) in  
328 2004 is the same as that in 2005 but larger than that in 2012, which suggests that self-sealing was still in  
329 progress from 2005 to 2012. In terms of geometric hydraulic conductivity  $k_g$ , the results measured in 2004  
330 are almost identical to those obtained in 2005 and 2012.

331 To apply the proposed damage model to the hydraulic conductivity, parameter  $a$  is taken the same as that  
332 used for the predictions of thermal conductivity and small strain shear modulus. By contrast, parameter  $b$   
333 is taken equal to -0.5 because the hydraulic conductivity increases with the increase of macro-pores. All  
334 the calculated values ( $k_{\perp}$ ,  $k_{//}$ ) are then compared to those measured in situ (Figure 11). It is observed that  
335 the predicted results are closer to those of the measurements of 2012 as compared with the  
336 measurements of 2004 and 2005. This is logic because the values of  $e_M$  are determined on samples taken  
337 in 2012.

338 The good agreement obtained between the model prediction and experimental data for the thermal  
339 conductivity (Figure 3), small-strain shear modulus (Figure 4) and hydraulic conductivity (Figure 11) shows  
340 that the damage variable defined based on the volume of macro-pores is relevant in predicting the effect  
341 of EDZ on the thermo-hydro-mechanical properties of natural Boom Clay.

## 342 **5. Discussion**

343 Experimental methods aiming at understanding the properties of stiff clay/soft rock in the EDZ often rely  
344 on in-situ identification, such as the ultrasonic velocity measurement used for Callovo-Oxfordian claystone  
345 (Schuster and Alheid, 2007), Boom Clay (Mertens et al., 2004), and Opalinus Clay (Martin Derek et al.,  
346 2003), the hydraulic conductivity measurement used for Boom Clay (Yu et al., 2011), Opalinus Clay  
347 (Martin Derek et al., 2003), etc. In this study, the measurements of small-strain shear modulus ( $G_0$ ) and of  
348 thermal conductivity ( $\lambda$ ) were undertaken in the laboratory to quantify the extent of EDZ in Boom Clay.  
349 From these measurements, it has been observed that the experimental data of  $\lambda$  and  $G_0$  follows the same  
350 evolution law with the distance  $r$  from the gallery. -. By contrast, within the EDZ, there is a drastic  
351 decrease in its hydro-mechanical performance. This is confirmed by the evolution of hydraulic property  
352 reported by Yu et al. (2011): a higher value was obtained in the EDZ as compared to the zone outside the  
353 EDZ. The presence of EDZ around Boom Clay formation was also confirmed through the in-situ  
354 measurement of compressional wave velocity ( $V_p$ ) by Mertens et al. (2004). Unfortunately, the boreholes

355 used to measure  $V_p$  in the study of Mertens et al. (2004) are not perpendicular to the connecting gallery,  
356 thus the interpretation of data is not straightforward.

357 As for the experimental methods of EDZ identification, the fracture/damage induced by excavation can be  
358 identified by mapping excavation surfaces (Lanyon, 2011). Following up this method, a method of tunnel  
359 crossing excavation that cut into the side-wall of the previously excavated tunnels was used (Martin and  
360 Lanyon, 2004) to detect the extent of EDZ in Opalinus Clay. As for the numerical approaches, there are  
361 several methods to predict the extent of EDZ using finite elements, explicit finite difference, distinct  
362 element, etc. To simulate the soil damage (fracture growth), a damage variable (usually called  $D$ ) is used  
363 which is derived from the test results of axial stress and strain, tangential strain, Young's modulus and  
364 Poisson's ratio (Hudson, 2009). In this study, the fractures which have the plate and parallel opening  
365 form observed at a microscopic scale were considered. Firstly, the global void ratio ( $e$ ) of the samples  
366 taken near and far the gallery was checked to detect the influence of fractures due to excavation on  $e_0$ .  
367 Table 1 shows that the values of  $e$  of the three samples are almost the same, suggesting that  $e_0$  is not an  
368 indicator of excavation damage. Then, the microstructure investigation of these samples was carried out,  
369 allowing the definition of a relevant damage parameter that is the ratio of the global void ratio ( $e_0$ ) to the  
370 void ratio of macro-pores (pore diameter  $\geq 5 \mu\text{m}$ ) ( $e_M$ ). When the soil is in the EDZ, there are more macro-  
371 pores, giving rise to larger values of  $e_M$ . Note that the applicability of this model is related to crack form  
372 openings. When the lower damage limit is reached (i.e. undamaged state), the value of  $e_M$  is very small  
373 and  $X$  is considered to be equal to  $X_0$ . When the upper damage limit is reached (i.e. totally damaged  
374 state), the value of  $e_M$  is very high and  $e/e_M \approx 0$ , hence  $X \approx 0$ .

375 As the values of  $e_0$  for all the three samples are around 0.64, the damage variable ( $e/e_M$ ) depend only on  
376  $e_M$ .

377 Figure 3, Figure 4, and Figure 11 show some differences between the experimental and prediction results.  
378 These differences are due to the chosen values of parameters  $a$  and  $b$  and the far field values of thermal  
379 conductivity, small-strain modulus and hydraulic conductivity (Table 2). In terms of thermal conductivity,  
380 the chosen far field values of  $\lambda_{//}$  (1.65 W/(m.K)) and  $\lambda_{45}$  (1.5 W/(m.K)) allow the predictions close to the  
381 experimental data. But for  $\lambda_{\perp}$ , the trend of experimental data is not regular due to the low values measured  
382 on the samples of far field: it increases to 1.05 W/(m.K) at  $r = 6.0$  m then decreases to 0.95 W/(m.K) at  $r =$   
383 20.8 m . Comparing to the value of  $\lambda_{\perp} = 1.31$  W/(m.K) obtained by Chen et al. (2011) by back-analysis, a  
384 far field value of  $\lambda_{\perp} = 1.1$  W/(m.K) was chosen.

385 In the case of small-strain modulus, the far field values of  $G_{hv}$ ,  $G_{h45}$ ,  $G_{hh}$  are more difficult to choose  
386 because the measurements by bender element always show some experimental data scatters. Among the  
387 three parameters measured ( $V_{hv}$ ,  $V_{hh}$  and  $V_{h45}$ ), it seems that  $V_{h45}$  is the most difficult to measure. There  
388 are several sources that may affect the accuracy of the measurement: identification of the bedding plane,  
389 contact between transmitter/receiver and the soil specimen, etc. The final far field values of  $G_{hv}$ ,  $G_{h45}$ ,  $G_{hh}$   
390 were chosen after comparing the measurements in this study and the values proposed by Lima (2011)  
391 under unconfined conditions.

392 In terms of hydraulic conductivity, the in-situ data showed the far field value clearly, but the predicted  
393 results under-estimate the values in EDZ, especially in the case parallel to the bedding plane  $k_{//}$  with the  
394 measurements conducted in 2004 and 2005 (Figure 11). As mentioned before, this is because parameters  
395  $a$  and  $b$  are determined based on the measurements on the samples from the borehole drilled in July  
396 2012, with the values of  $e_M$  that must be lower than those in 2004 and 2005, due to the self-sealing  
397 capacity of Boom Clay. The decrease of  $e_M$  over time is related to the decrease of the dimensions of  
398 cracks identified in Figures 8 and 9. The large difference between the predicted results and the data of  
399 2004 and 2005 shows that parameters  $a$  and  $b$  change over time. In other words, a given set of  
400 parameters corresponds to a given time, and the proposed model can be used to estimate the effect of  
401 EDZ only for this given time.

402

## 403 **6. Conclusions**

404 This study aimed at investigating the influence of EDZ around the connecting gallery on the thermal  
405 conductivity, small strain modulus and hydraulic conductivity. Several samples of natural Boom Clay at  
406 different distances from the gallery were taken from the borecore drilled in July 2012, and thermal  
407 conductivity and bender element tests were carried out on these samples. As Boom Clay is a cross-  
408 anisotropic material, the anisotropy of its properties was investigated by considering different directions  
409 with respect to the bedding plane. Microstructural observations were also made using MIP and SEM  
410 methods on the samples located at different distances from the gallery. The identified macro-pores were  
411 related to the effect of excavation damage, and a damage variable was thus defined, allowing the  
412 properties of Boom Clay to be estimated.

413 In terms of thermal measurements, the thermal conductivity ( $\lambda$ ) in three directions - parallel ( $\lambda_{//}$ ),  
414 perpendicular ( $\lambda_{\perp}$ ), and inclined  $45^\circ$  ( $\lambda_{45}$ ) to the bedding plane was measured using the needle probe  
415 method. The results showed the same evolution with the distance  $r$  from the gallery axis in the three  
416 orientations: in the zone far from the gallery, the thermal conductivity stabilises then it drops down to lower  
417 values while  $r < 4$  m. An extent of EDZ about 4 m from the gallery axis (1.6 m from the gallery extrados)  
418 was identified.

419 The mechanical property of Boom Clay around the connecting gallery was investigated through the  
420 measurements of the small-strain shear modulus ( $G_0$ ) by bender element under unconfined conditions.  
421 The values in three directions  $G_{hv}$ ,  $G_{h45}$ ,  $G_{hh}$  were determined on samples at several distances  $r$ . Although  
422 the experimental results are not as regular as those for the thermal conductivity, an extent of EDZ of about  
423 4 m from the gallery axis was also identified.

424 The MIP tests revealed that the samples close to the gallery's wall have macro-pores larger than  $5 \mu\text{m}$ .  
425 These pores correspond to cracks observed at the SEM observations, and can be related to the  
426 excavation damage.

427 From the void ratio of macro-pore  $e_M$  obtained from the MIP tests, a damage variable was defined and a  
428 damage model was proposed allowing the prediction of the thermal-hydro-mechanical properties of Boom  
429 Clay around the gallery. This model was validated by comparing the predicted and experimental results in  
430 terms of thermal conductivity and small-strain shear modulus in different orientations, with the same  
431 parameters  $a$  and  $b$ . Further analysis was conducted in terms of hydraulic conductivity. It was observed  
432 that satisfactory prediction was obtained for the year 2012 where both the hydraulic conductivity  
433 measurement and the sampling for  $e_M$  determination were done. The results also suggest that parameters  
434  $a$  and  $b$  may change over time because of the self-sealing capacity of Boom Clay that leads to a decrease  
435 of  $e_M$  over time.

436

## 437 **Acknowledgements**

438 The authors would like to express their gratitude to Ecole des Ponts ParisTech (ENPC), European  
439 Underground Research Infrastructure for Disposal of nuclear waste In Clay Environment (EURIDICE) and  
440 Belgian Agency for Radioactive Waste and Enriched Fissile Materials (ONDRAF/NIRAS) for their financial  
441 supports.

442

## 443 **References**

- 444 Ambroziak, A., 2007. Identification and validation of damage parameters for elsto-viscoplastic chaboche  
445 model. Eng. Trans. 55, 3–28.
- 446 Areias, L., Verstricht, J., Fischer, T., Philipp, J., 2012. Seismic Monitoring at the Underground Nuclear  
447 Research Laboratory in MOL, Belgium - 12461, in: WM2012 Conference. Phoenix, Arizona, USA.
- 448 Armand, G., Lebon, P., Cruchaudet, M., Rebours, H., Morel, J., Wileveau, Y., Agence, A.-, De, L., Meuse,  
449 D., Marne, H., Cedex, C., 2007. EDZ Characterisation in the Meuse / Haute-Marne Underground  
450 Research Laboratory, in: Clays in Natural & Engineered Barriers for Radioactive Waste  
451 Confinement. International meeting, September 17-18 2007, Lille, France, pp. 153–154.
- 452 Autio, J., Siitari-Kauppi, M., Timonenc, J., Hartikainen, K., Hartikainen, J., 1998. Determination of the  
453 porosity, permeability and diffusivity of rock in the excavation-disturbed zone around full-scale  
454 deposition holes using the View the C14-PMMA and He-gas methods. J. Contam. Hydrol. 35, 19–29.
- 455 Bastiaens, W., Bernier, F., Buyens, M., Demarche, M., Li, X.L., Linotte, J.M. and Verstricht, J., 2003. The  
456 Connecting Gallery - the extension of the HADES underground research facility at Mol, Belgium.  
457 EURIDICE report 03-294. Mol: ESV EURIDICE.
- 458 Bernier, F., Li, X.L., Bastiaens, W., Ortiz, L., Van Geet, M., Wouters, L., Frieg, B., Blümling, P., Desrues,  
459 J., Viaggiani, G., Coll, C., Chanchole, S., De Greef, V., Hamza, R., Malinsky, L., Vervoort, A.,  
460 Vanbrabant, Y., Debecker, B., Verstraelen, J., Govaerts, A., Wevers, M., Labiouse, V., Escoffier, S.,  
461 Mathier, J.F., Gastaldo, L. and Bühler, Ch., 2006. Fractures and self-healing within the excavation  
462 disturbed zone in clays. EC report on the SELFRAC project.

- 463 Bernier, F., Li, X.L., Bastiaens, W., 2007. Twenty-five years' geotechnical observation and testing in the  
464 Tertiary Boom Clay formation. *Géotechnique* 57, 229–237.
- 465 Charlier, R., Collin, F., Dizier, A., Fauriel, S., Gens, A., Guangjing, C., Laloui, L., Meynet, T., Pascon, F.,  
466 Radu, J.P., Marcke, P., Vaunat, J., 2010. Thermal Impact on the Damaged Zone Deliverable D13 –  
467 Annex 6 Large scale excavation and heater in-situ experiment : the PRACLAY experiment  
468 modelling.
- 469 Chen, G.J., Sillen, X., Verstricht, J., Li, X.L., 2011. ATLAS III in situ heating test in boom clay: Field data,  
470 observation and interpretation. *Comput. Geotech.* 38, 683–696.
- 471 Das, B.M., 1983. *Advanced Soil Mechanics*. Hemisphere Publishing Corp.
- 472 Dehandschutter, B., Vandycke, S., Sintubin, M., Vandenberghe, N., Wouters, L., 2005. Brittle fractures  
473 and ductile shear bands in argillaceous sediments: inferences from Oligocene Boom Clay (Belgium).  
474 *J. Struct. Geol.* 27, 1095–1112.
- 475 Delage, P., Pellerin, F.M., 1984. Influence de la lyophilisation sur la structure d'une argile sensible du  
476 Québec. *Clays Miner.* 19, 151–160.
- 477 Delage, P., Le, T.T., Tang, A.M., Cui, Y.J., Li, X.L., 2007. Suction effects in deep Boom Clay block  
478 samples. *Géotechnique* 57, 239–244.
- 479 Diamond, S., 1970. Pore size distribution in clays. *Clays Clay Min.* 18, 7–23.
- 480 Farouki, O.T., 1986. *Thermal properties of soils*. Trans Tech Publications, Clausthal-Zellerfeld, Germany.
- 481 Gross, D., Seelig, T., 2011. Damage mechanics, in: *Fracture Mechanics SE - 9*. Springer Berlin  
482 Heidelberg, pp. 301–316.
- 483 Hudson, J.A., 2009. Characterising and modelling the excavation damaged zone ( EDZ ) in crystalline  
484 rock in the context of radioactive waste disposal. Lawrence Berkeley Natl. Lab.
- 485 Kachanov, L., 1958. Time of the rupture process under creep conditions. *TVZ Akad Nauk S.S.R Otd.*  
486 *Tech. Nauk* 8, 26–31.
- 487 Lanyon, G., 2011. Excavation Damaged Zones Assessment, OPG's Deep Geologic Respository for Low  
488 & Intermediate waste. Report of Fracture Systems Ltd - NWMO DGR-TR-2011-21.
- 489 Le, T.T., 2008. Comportement thermo-hydro-mécanique de l'argile de Boom. PhD. Ecole Nationale des  
490 Ponts et Chaussées.
- 491 Lima, A., 2011. Thermo-hydro-mechanical behaviour of two deep Belgian clay formations: Boom and  
492 Ypersian Clays. PhD thesis. Universitat Politècnica de Catalunya.
- 493 Martin, C., Lanyon, G.W., 2004. Excavation Disturbed Zone (EDZ) in Clay Shale: Mont Terri.
- 494 Martin Derek, C., Lanyon, G.W., Blümling, P., Mayor, J., 2003. The excavation disturbed zone around a  
495 test tunnel in the Opalinus Clay. *Tunn. Assoc. Canada Annu. Publ.*
- 496 Matray, J.M., Savoye, S., Cabrera, J., 2007. Desaturation and structure relationships around drifts  
497 excavated in the well-compacted Tournemire's argillite (Aveyron, France). *Eng. Geol.* 90, 1–16.
- 498 Mertens, J., Bastiaens, W., Dehandschutter, B., 2004. Characterisation of induced discontinuities in the  
499 Boom Clay around the underground excavations (URF, Mol, Belgium). *Appl. Clay Sci.* 26, 413–428.



- 500 Mertens, J., Vandenberghe, N., Wouters, L., Sintubin, M., 2003. The origin and development of joints in  
501 the Boom Clay Formation (Rupelian) in Belgium. *Geol. Soc. London, Spec. Publ.* 216 , 309–321.
- 502 Mertens, J., Bastiaens, W., Dehandschutter, B., 2002. Characterisation of induced discontinuities in the  
503 Boom Clay around the underground excavations (URF, Mol, Belgium), in: *Clays in Natural &*  
504 *Engineered Barriers for Radioactive Waste Confinement.* pp. 43–44.
- 505 Nguyen, X.P., 2013. Étude du comportement chimico-hydro- mécanique des argiles raides dans le  
506 contexte du stockage de déchets radioactifs. PhD thesis. Université Paris-Est.
- 507 Penner, E., 1963. Anisotropic thermal conduction in clay sediments, in: *International Clay Conference.*
- 508 Popp, T., Salzer, K., Minkley, W., 2008. Influence of bedding planes to EDZ-evolution and the coupled HM  
509 properties of Opalinus Clay. *Phys. Chem. Earth* 33, S374–S387.
- 510 Romero, E., 1999. Characterisation and thermo-hydro-mechanical behaviour of unsaturated Boom Clay:  
511 An experimental study. *Universitat Politècnica de Catalunya.*
- 512 Roy, P., 1991. Measurements of soil permeability anisotropy by three techniques. Thesis. McGill  
513 University (Montreal).
- 514 Schuster, K., Alheid, H.J., 2007. EDZ characterisation with ultrasonic interval velocity measurements in  
515 the URL Meuse/Haute-Marne -performed between depth of 85 m and 504 m, in: *International*  
516 *Meeting “Clay in Natural & Engineered Barriers for Radioactive Waste Confinement”.* September 17-  
517 18, Lille, France, pp. 155–156.
- 518 Tang, A.M., Cui, Y.J., Le, T.T., 2008. A study on the thermal conductivity of compacted bentonites. *Appl.*  
519 *Clay Sci.* 41, 181–189.
- 520 Tsang, C.F., Bernier, F., 2004. Definitions of excavation disturbed zone and excavation damaged zone, in  
521 Impact of the excavation disturbed or damaged zone (EDZ) on the performance of radioactive waste  
522 geological repositories, in: *Proceedings European Commission CLUSTER Conference and*  
523 *Workshop on EDZ in Radioactive Waste Geological Repositories.* Luxembourg, Belgium.
- 524 Tsang, C.F., Bernier, F., Davies, C., 2005. Geohydromechanical processes in the Excavation Damaged  
525 Zone in crystalline rock, rock salt, and indurated and plastic clays- in the context of radioactive waste  
526 disposal. *Int. J. Rock Mech. Min. Sci.* 42, 109–125.
- 527 Yu, L., Gedeon, M., Wemaere, I., Marivoet, J., De Craen, M., 2011a. Boom Clay Hydraulic Conductivity. A  
528 synthesis of 30 years of research. External report SCK-CEN, Mol (Belgium).
- 529 Yu, L., Weetjens, E., Vietor, T., 2011b. Integration of TIMODAZ Results within the Safety Case and  
530 Recommendations for Repository Design.
- 531 Yu, L., Rogiers, B., Gedeon, M., Marivoet, J., Craen, M. De, Mallants, D., 2013. A critical review of  
532 laboratory and in-situ hydraulic conductivity measurements for the Boom Clay in Belgium. *Appl. Clay*  
533 *Sci.* 75-76, 1–12.
- 534 Zeng, X., Ni, B., 1999. Stress-Induced anisotropic Gmax of sands and its measurement. *J. Geotech.*  
535 *Geoenvironmental Eng.* 125, 741–749.

536

537 **List of Tables**

538 Table 1: Physical and thermo-mechanical properties of natural Boom Clay.  $r$ : distance from the axis of  
539 gallery,  $w$ : water content (%),  $\rho$ : total density of the soil,  $\lambda$ : thermal conductivity,  $G$ : small-strain shear  
540 modulus,  $e$ : void ratio;  $e_M$ : void ratio of macro-pores.

541 Table 2: Parameters used for model predictions.

542

## 543 **List of Figures**

544 Figure 1: Measurement of thermal conductivity by needle probe method in the laboratory.

545 Figure 2: Measurement of shear wave velocity by bender element method in the laboratory (the three  
546 arrows indicate the directions of particle vibration).

547 Figure 3: Comparison of shear modulus between model and experiment.

548 Figure 4: Comparison of thermal conductivity between model and experiment.

549 Figure 5: Bedding plane on natural Boom Clay sample.

550 Figure 6: Pore size distributions of three Boom Clay samples located at different distances from the axis of  
551 gallery  $r$ .

552 Figure 7: Void ratio of macro-pores  $e_M$  at different distances from the axis of gallery  $r$ .

553 Figure 8: SEM images viewing perpendicular (a) and parallel (b) to the bedding plane for the sample  
554 located at  $r = 2.5$  m; (a) picture scale:  $1800 \times 1400 \mu\text{m}$  and (b) picture scale:  $1500 \times 1100 \mu\text{m}$ .

555 Figure 9: SEM images viewing perpendicular (a) and parallel (b) to the bedding plane for the sample  
556 located at  $r = 2.7$  m : (a) picture scale:  $2550 \times 1950 \mu\text{m}$  and (b) picture scale:  $850 \times 650 \mu\text{m}$ .

557 Figure 10: SEM images viewing perpendicular (a) and parallel to the bedding plane (b) for the sample  
558 located at  $r = 9.2$  m: (a) picture scale:  $2300 \times 1800 \mu\text{m}$  and (b) picture scale:  $640 \times 500 \mu\text{m}$ .

559 Figure 11: Comparison of hydraulic conductivity between the field measurements and model predictions.

560

561

562 Table 1: Physical and thermo-mechanical properties of natural Boom Clay.  $r$ : distance from the axis of  
 563 gallery,  $w$ : water content (%),  $\rho$ : total density of the soil,  $\lambda$ : thermal conductivity,  $G$ : small-strain shear  
 564 modulus,  $e$ : void ratio;  $e_M$ : void ratio of macro-pores.

Distance $r$ (m)	$w$ (%)	$\rho$ (Mg/m <sup>3</sup> )	$e$	$\lambda_{\perp}$ (W/(m.K))	$\lambda_{45}$ (W/(m.K))	$\lambda_{//}$ (W/(m.K))	$G_{hv}$ (MPa)	$G_{h45}$ (MPa)	$G_{hh}$ (MPa)	$e/e_M$
2.5	20.7	1.97	0.65	0.898	1.267	1.341	807.85	1065.9	819.3	12.395
2.7	21.3	1.97	0.64	0.818	1.230	1.421	637.55	1369.3	1197.8	26.326
9.2	20.3	1.95	0.64	0.941	1.477	1.605	1206.77	1357.5	1197.8	67.107

565

566

567

568

569 Table 2: Parameters used for model predictions.

Property $X$	$X_0$
$G_{hv}$ (MPa)	1100
$G_{h45}$ (MPa)	1300
$G_{hh}$ (MPa)	1450
$V_p$ (m/s)	1930
$k_{\perp} \times 10^{-14}$ (m/s)	350
$k_{//} \times 10^{-14}$ (m/s)	650
$\lambda_{//} \times 10^{-3}$ (W/(m.K))	1650
$\lambda_{45} \times 10^{-3}$ (W/(m.K))	1500
$\lambda_{\perp} \times 10^{-3}$ (W/(m.K))	1100

570

571

572

573

574

575

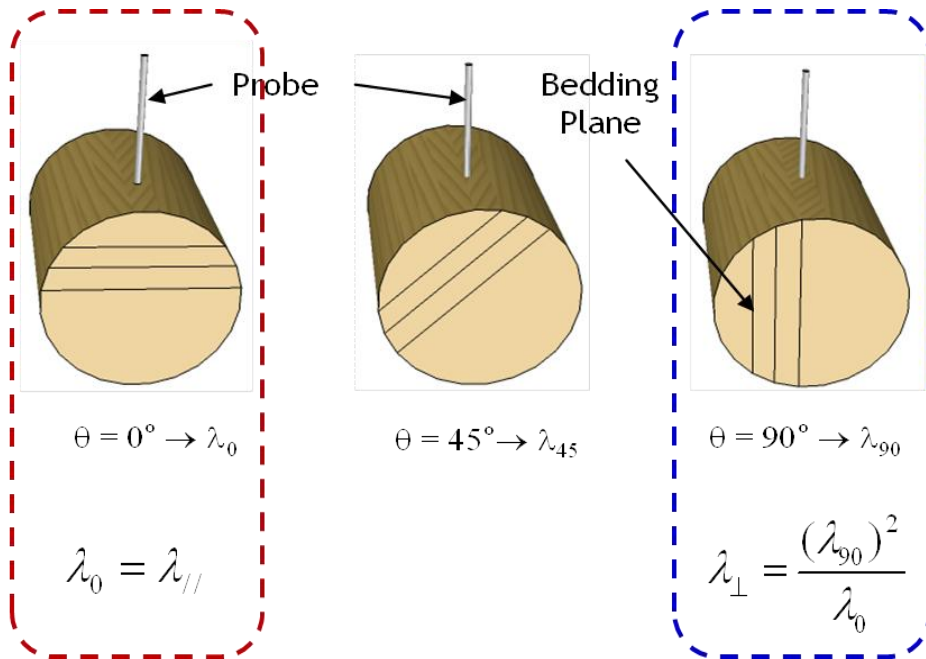
576

577

578

579

580



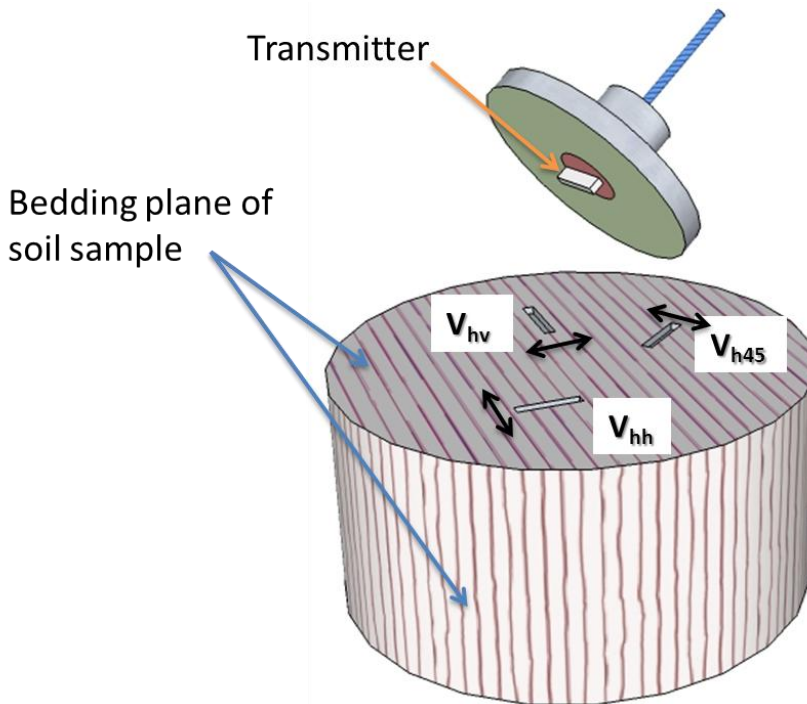
581

582

583 Figure 1: Measurement of thermal conductivity by needle probe method in the laboratory.

584

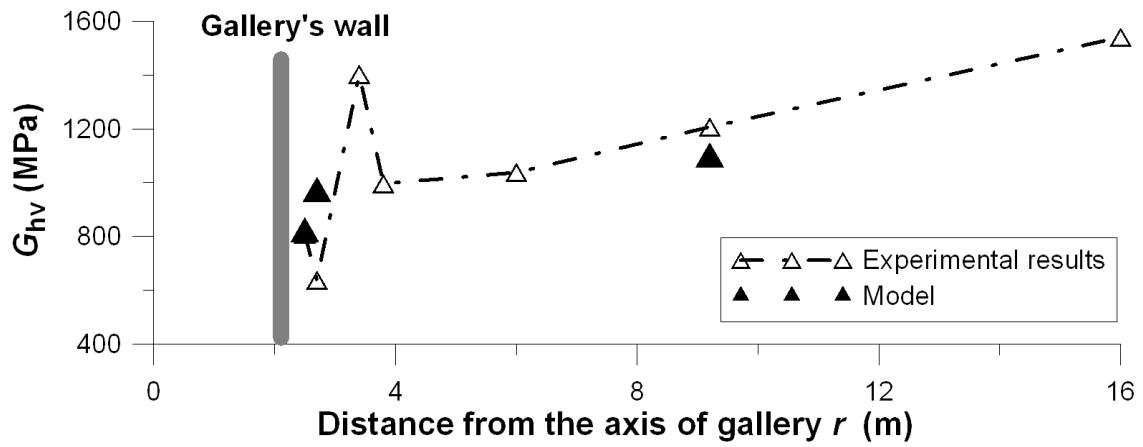
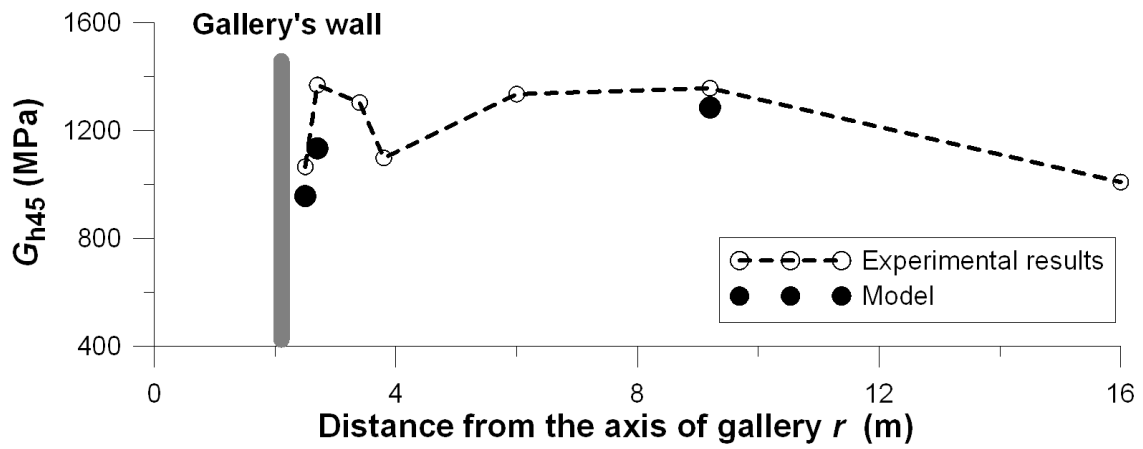
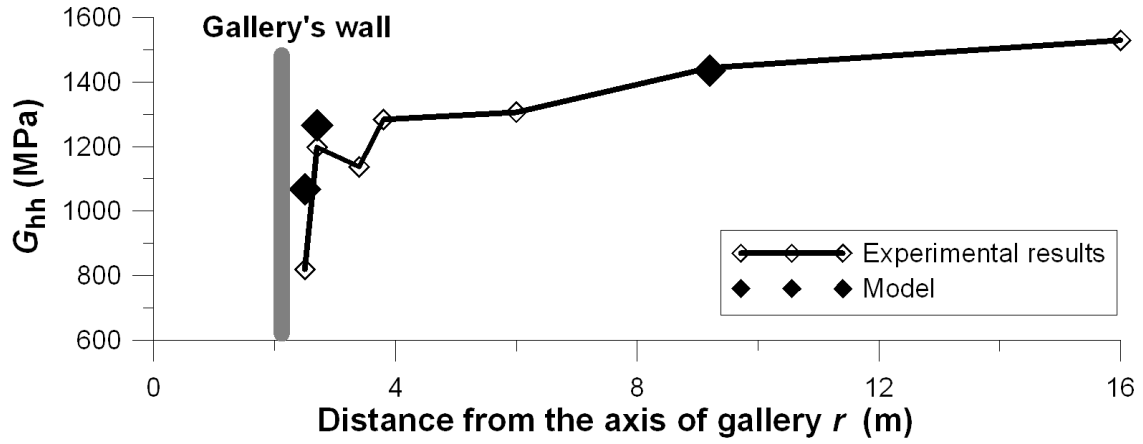
585



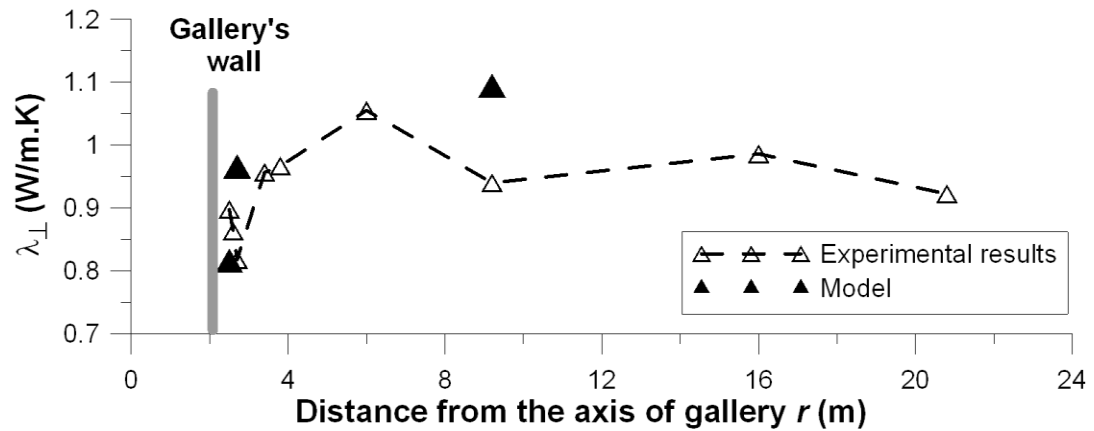
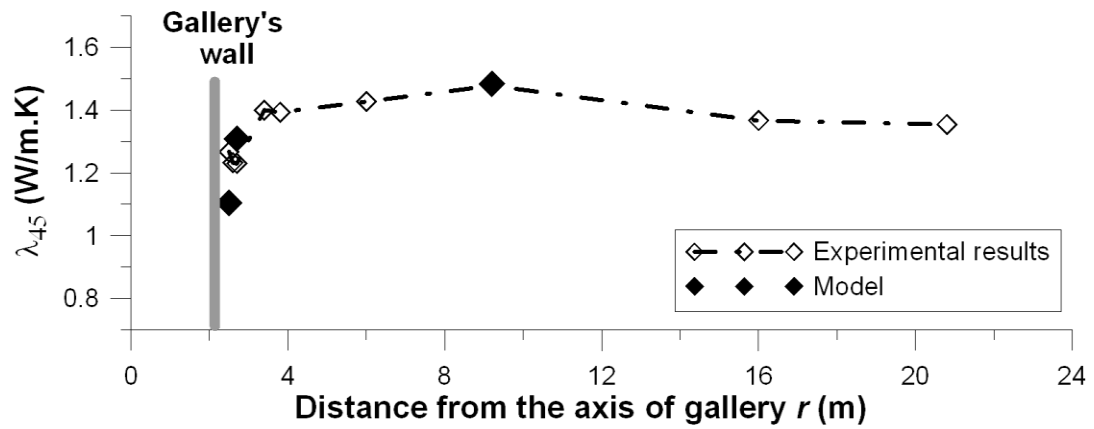
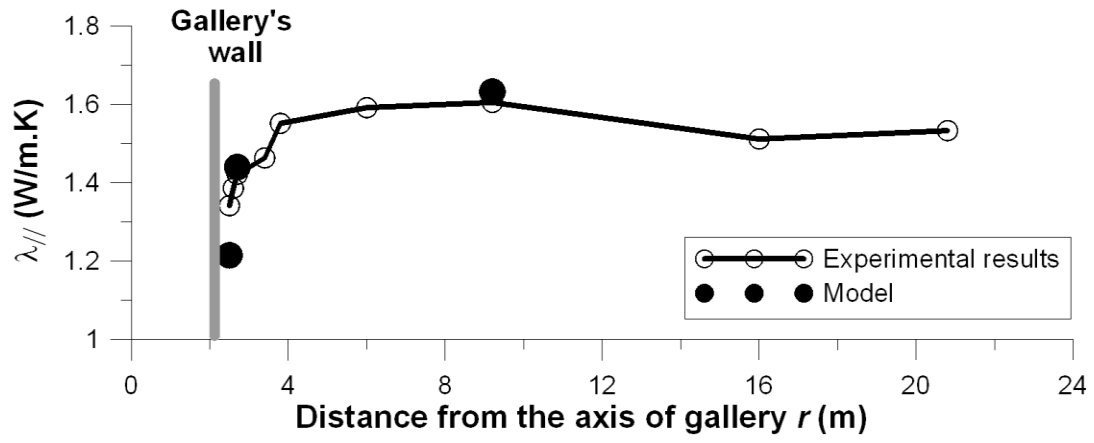
586

587 Figure 2: Measurement of shear wave velocity by bender element method in the laboratory (the three  
588 arrows indicate the directions of particle vibration).

589



592 Figure 3: Comparison of shear modulus between model and experiment.



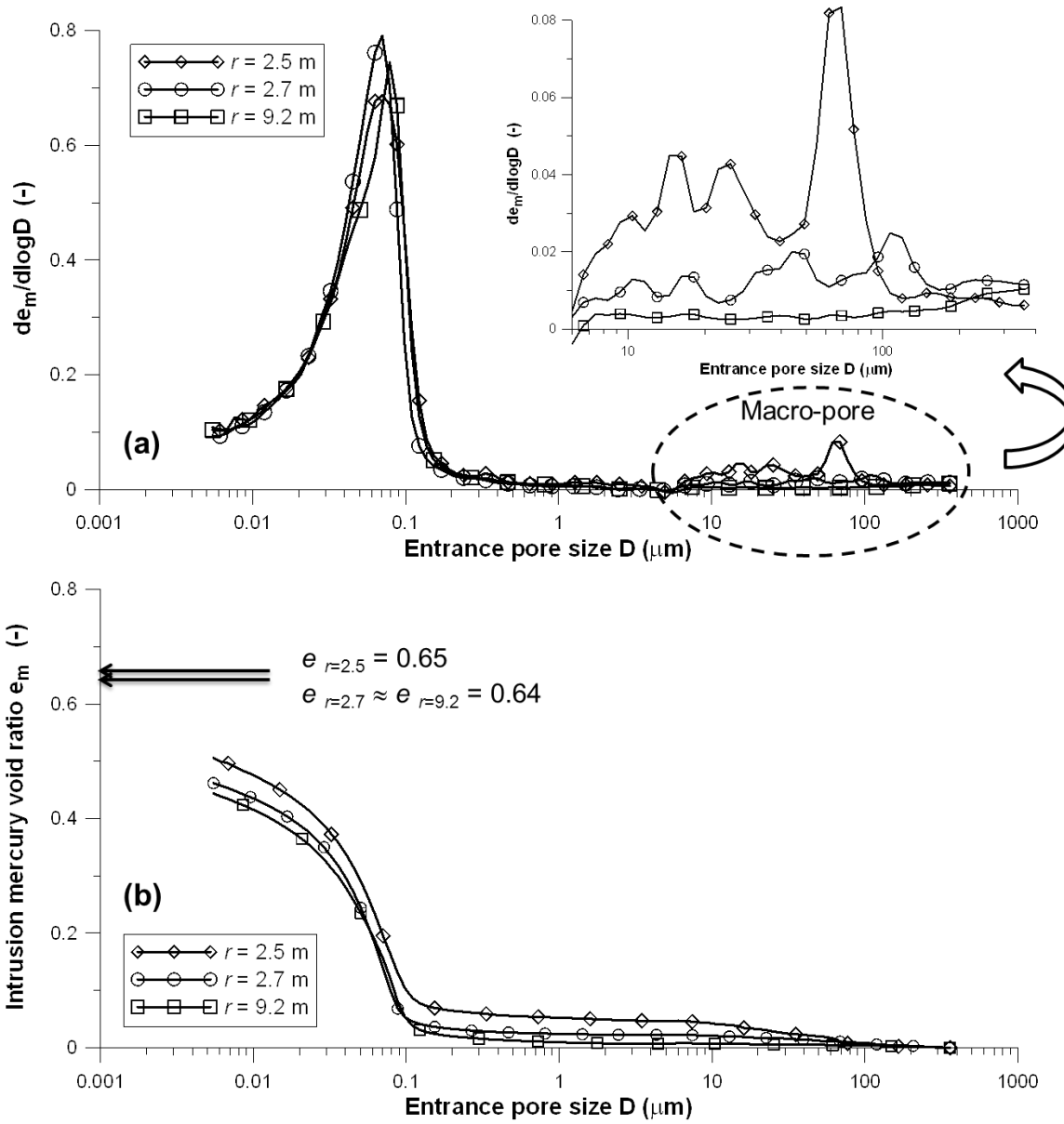
594  
 595  
 596  
 597  
 598  
 599  
 600

Figure 4: Comparison of thermal conductivity between model and experiment.



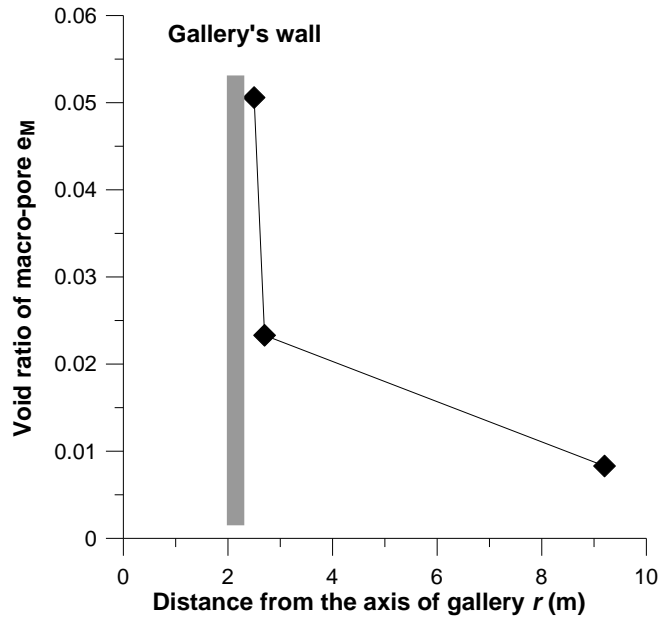
601  
602 Figure 5: Bedding plane on natural Boom Clay sample.

603



604  
605 Figure 6: Pore size distributions of three Boom Clay samples located at different distances from the axis of  
606 gallery  $r$ .

607

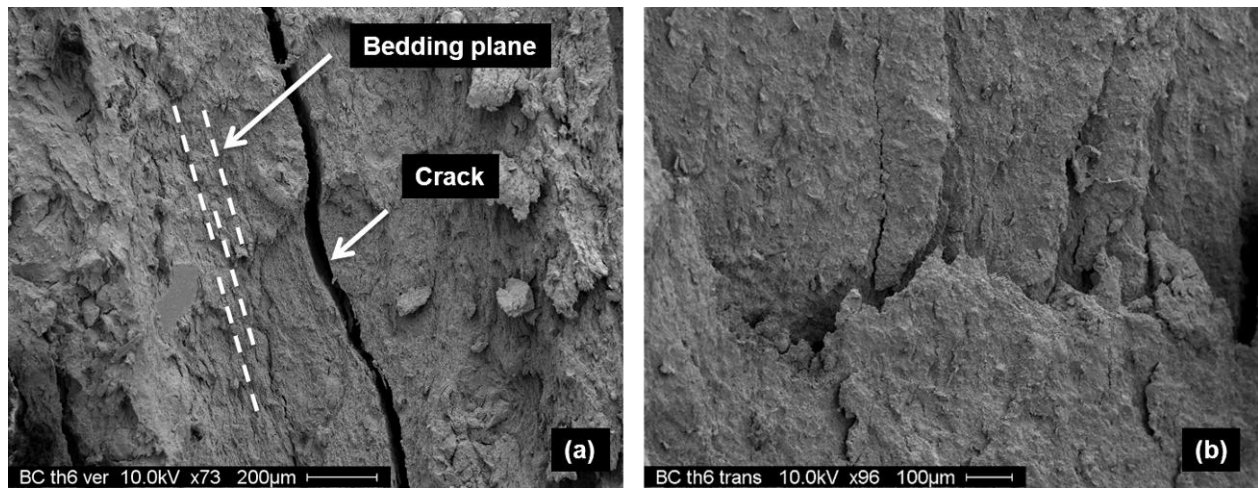


608

609 Figure 7: Void ratio of macro-pores  $e_M$  at different distances from the axis of gallery  $r$ .

610

611

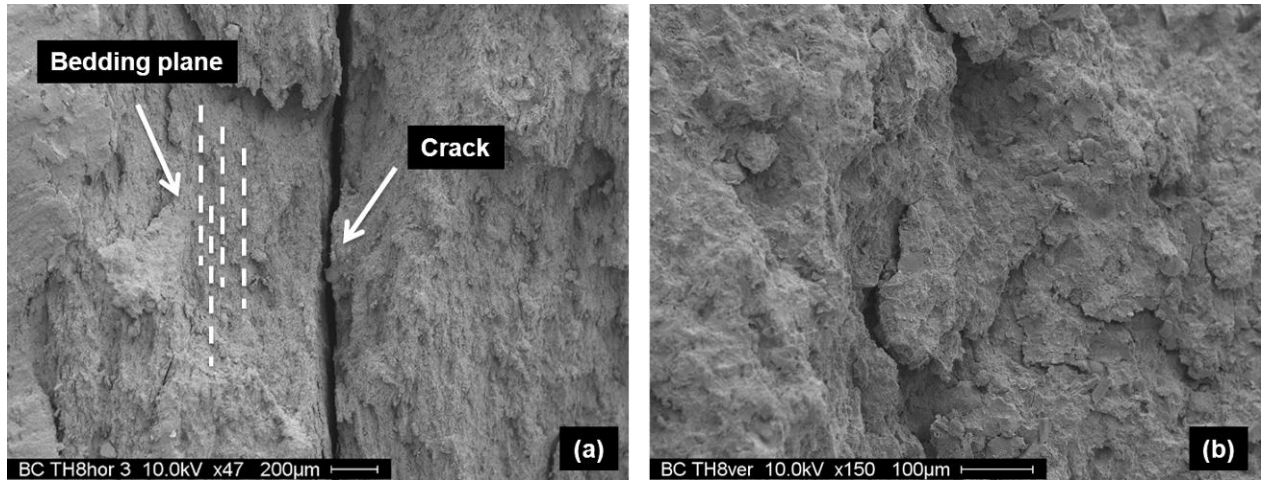


612  
613

614 Figure 8: SEM images viewing perpendicular (a) and parallel (b) to the bedding plane for the sample  
615 located at  $r = 2.5$  m; (a) picture scale: 1800 x 1400  $\mu\text{m}$  and (b) picture scale: 1500 x 1100  $\mu\text{m}$ .

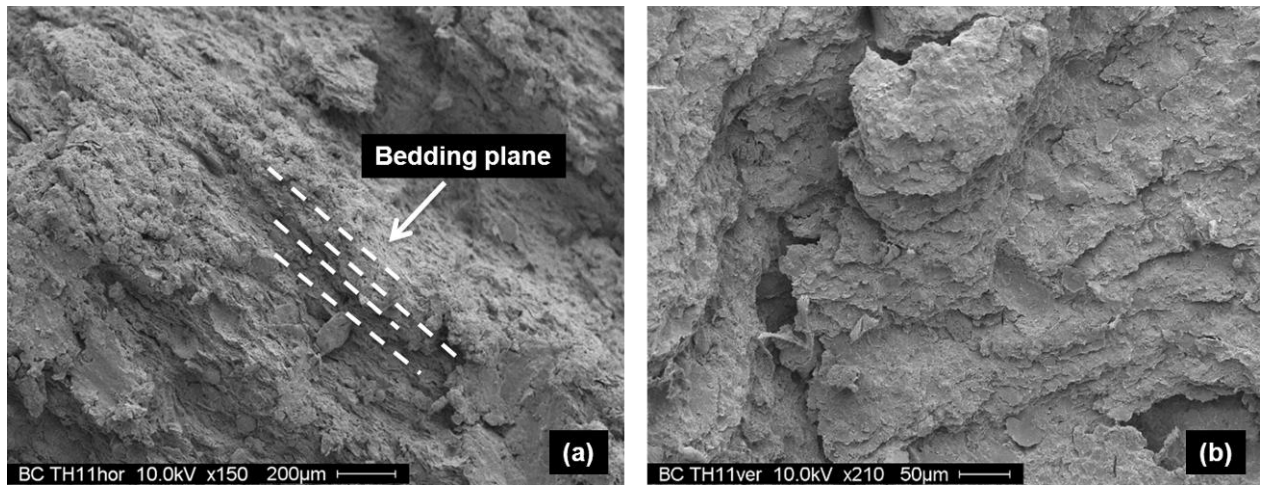
616





617  
 618 Figure 9: SEM images viewing perpendicular (a) and parallel (b) to the bedding plane for the sample  
 619 located at  $r = 2.7$  m : (a) picture scale: 2550 x 1950  $\mu\text{m}$  and (b) picture scale: 850 x 650  $\mu\text{m}$ .

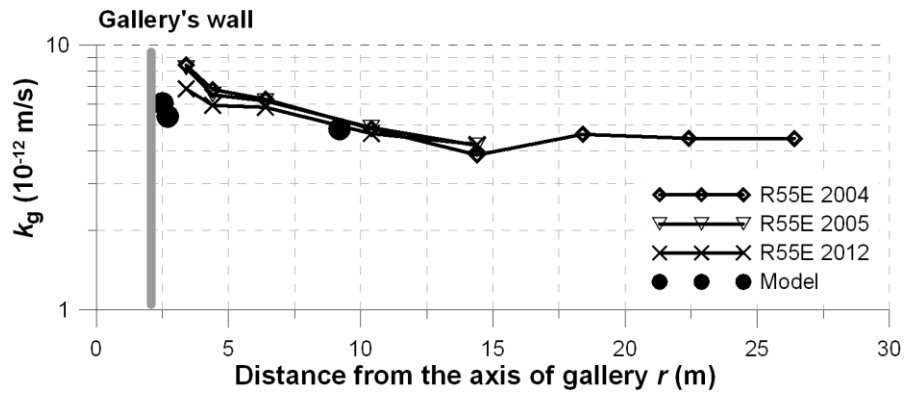
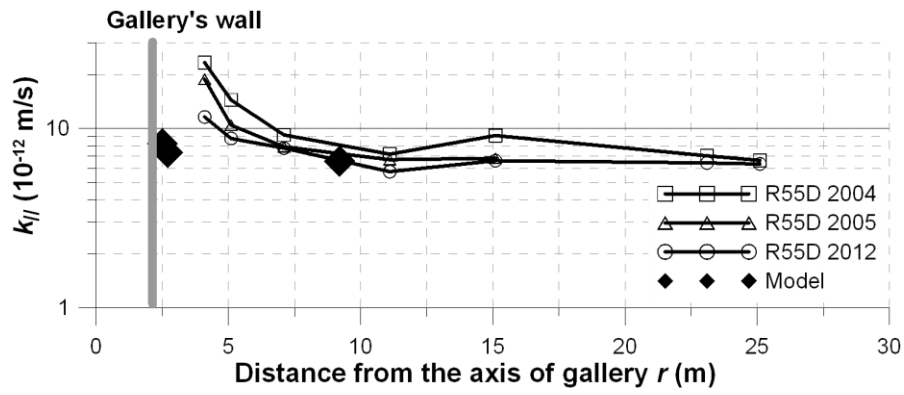
620



621  
 622 Figure 10: SEM images viewing perpendicular (a) and parallel to the bedding plane (b) for the sample  
 623 located at  $r = 9.2$  m: (a) picture scale: 2300 x 1800  $\mu\text{m}$  and (b) picture scale: 640 x 500  $\mu\text{m}$ .

624

625



626

627 Figure 11: Comparison of hydraulic conductivity between the field measurements and model predictions.